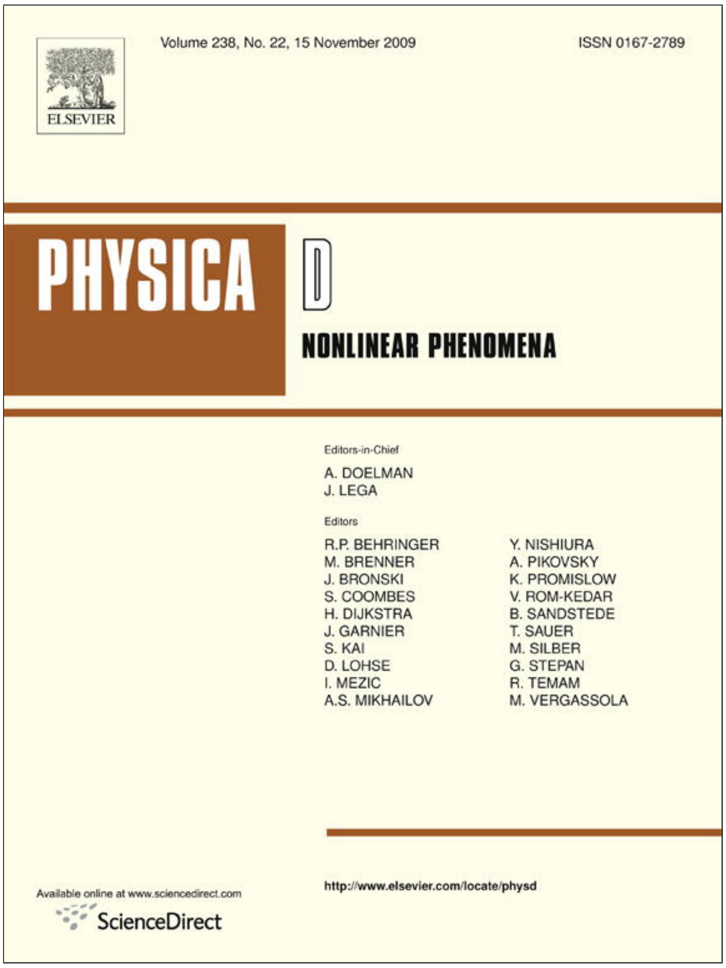

Volume 238, No. 22, 15 November 2009 ISSN 0167-2789

ELSEVIER

PHYSICA D

NONLINEAR PHENOMENA

Available online at www.sciencedirect.com
ScienceDirect

http://www.elsevier.com/locate/physd

Physica D 238 (2009) 2153–2165

Contents lists available at ScienceDirect

Physica D

journal homepage: www.elsevier.com/locate/physd

Reverse draining of a magnetic soap film — Analysis and simulation of a thin film equation with non-uniform forcing

D.E. Moulton *, J. Lega

University of Arizona, Department of Mathematics, 617 N. Santa Rita, Tucson, AZ 85721, USA

ARTICLE INFO

Article history:
Received 23 March 2009
Received in revised form
28 June 2009
Accepted 18 August 2009
Available online 28 August 2009
Communicated by M. Brenner

Keywords:
Thin film equation
Equilibrium analysis
Soap film
Magnetic field
Lubrication approximation
Evolution equation

ABSTRACT

We analyze and classify equilibrium solutions of the one-dimensional thin film equation with no-flux boundary conditions and in the presence of a spatially dependent external forcing. We prove theorems that shed light on the nature of these equilibrium solutions, guarantee their validity, and describe how they depend on the properties of the external forcing. We then apply these results to the reverse draining of a one-dimensional magnetic soap film subject to an external non-uniform magnetic field. Numerical simulations illustrate the convergence of the solutions towards equilibrium configurations. We then present bifurcation diagrams for steady state solutions. We find that multiple stable equilibrium solutions exist for fixed parameters, and uncover a rich bifurcation structure to these solutions, demonstrating the complexity hidden in a relatively simple looking evolution equation. Finally, we provide a simulation describing how numerical solutions traverse the bifurcation diagram, as the amplitude of the forcing is slowly increased and then decreased.

1. Introduction

As a vertical soap film drains under gravity, a growing region of very thin film, termed black film, forms at the top. This process has been studied by a number of authors, and for a variety of reasons, including the capture of film properties, and the understanding of foams [1,2]. Much of the interest, with contributions dating as far back as Newton [3], seems to arise from the complexity underlying the process. The physical mechanisms behind a draining film have been analyzed and put in concrete mathematical terms in more recent times, largely beginning with the work of Mysels et al. in the 1950s [4]. In particular, they introduced the concept of marginal regeneration to explain the formation of thin regions of film along the film borders. Since then, multiple authors have added to the topic (e.g, [5–7]), both experimentally and theoretically.

The process of marginal regeneration, in particular the mechanisms responsible for the creation of black film at the film borders and the forces that drive the motion of the thin film once it is created, is still somewhat controversial. For instance, in [7] the authors suggest that the formation of thin film is a surface tension effect, contrary to the original explanation given by Mysels et al. In [8] the commonly held understanding that the thin film's subsequent motion is solely due to gravity is called into question. The dynamics of a draining film come from the competition between viscous, capillary, and gravitational forces, along with surface tension effects and potentially complex interactions with the film boundary. That some controversy remains today confirms that these systems which may at first appear relatively simple are actually quite complex.

One way to better understand a draining film and to capture the effects of different parameters is to add a controllable component to the system. In [9], Elias et al. explored the physical properties of soap films by adding an aqueous suspension of magnetic nanoparticles to an ordinary soap solution, thus forming a magnetic soap solution. This added magnetic dimension was treated as a macroscopic force which they could control by subjecting the film to varying magnetic fields. By placing a vertical draining film in a uniform magnetic field, they found that they could speed up or slow down the draining process based on the orientation of the magnetic field. More recently, Moulton and Pelesko [8] presented a similar experimental setup with a magnetic soap film, but with a key difference: they subjected a draining film to much stronger and non-uniform magnetic fields, by placing strong bar magnets above the vertical film. With this setup, they found that with a strong enough magnet, the film would flow upwards against gravity, with thin black film forming at the bottom, a process termed reverse draining.

In [8], a first model is suggested for the draining film under the presence of a non-uniform magnetic field. Numerical simulations demonstrate qualitative agreement with experimental observation, but a rigorous analysis of the system is not given. We provide such an analysis in this paper.

* Corresponding author. Tel.: +1 520 621 4835.
E-mail addresses: moulton@math.arizona.edu (D.E. Moulton), lega@math.arizona.edu (J. Lega).

0167-2789/$ – see front matter © 2009 Elsevier B.V. All rights reserved.
doi:10.1016/j.physd.2009.08.014

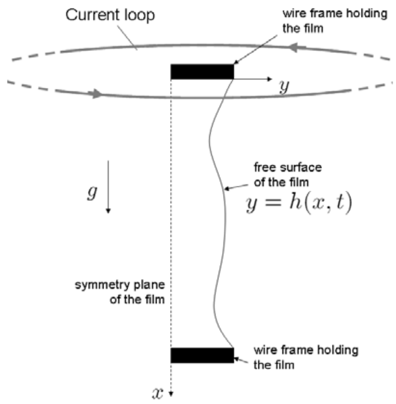

Fig. 1. Setup for the draining magnetic film system on which the model is based. See text for details.

The system we study is depicted in Fig. 1. The film is described by the function $y = h(x, t)$, which is the half-thickness of the film, assuming a reflection symmetry about the center line. The full film is envisioned by extending the profile in the transverse z direction — that is, the film is a sheet independent of z and with reflectional symmetry about $y = 0$. The film is assumed to be tangentially immobile, meaning that there is a zero tangential velocity along the free surface. The magnet is modeled by a current loop placed directly above the film, with the film sitting on the axis of the loop. The radius of the current loop is assumed to be much larger than the width of the film in the transverse z direction. This results in a non-uniform magnetic force acting only in the vertical x direction to first order, and models the effect that magnetic particles are primarily being pulled upwards, and that particles closer to the magnet will feel a stronger pull. To be physically realistic, a magnetic force acting solely in the vertical direction to first order is only compatible with the assumption that the film is uniform in the transverse z direction if the width of the film is small compared to the radius of the current loop, which may or may not agree with experiment. However, such a magnetic field is necessary in order to formulate a two-dimensional first model, which is certainly desirable from an analytical perspective. The model exploits several other simplifications, such as the absence of surfactant transport, in order to focus on the basic mechanism and effect of the magnetic field. Moreover, only macroscopic effects of the magnetic field are taken into account, and magnetic particle concentration is not considered. Nevertheless, we will see that this model has a very rich set of solutions, and is also capable of capturing the reverse draining effect observed in experiments.

An evolution equation for the film can be derived using lubrication theory, under the assumption of small aspect ratio of the thickness of the film to its length. A comprehensive review of lubrication theory and its application to various thin film systems is found in [10]. For the setup studied here, the fluid is assumed incompressible, with constant density and viscosity. Symmetry conditions are employed at the center line $y = 0$, while the assumption of a tangentially immobile film provides the boundary condition of zero velocity in the vertical x direction at the free surface. The effects of gravity, viscosity, and surface tension are included; a magnetic body force term also appears as described by the theory of ferrohydrodynamics [11]. Starting from the Navier–Stokes equations, and following the standard procedures, the following evolution equation for the film is obtained:

$$\frac{\partial h}{\partial t} + \frac{\partial}{\partial x}\left(\frac{h^3}{3}\left[\sigma h_{xxx} + 1 + \lambda f(x)\right]\right) = 0. \tag{1}$$

There are two dimensionless parameters: σ is an inverse Capillary number characterizing surface tension, while λ is a ratio of the relative forces of the magnetic field and gravity. Gravity has been scaled to be the factor of 1, and

$$f(x) = \frac{-3\eta^2 x}{(1+\eta^2 x^2)^4} \tag{2}$$

is the magnetic forcing function for the non-uniform magnetic field, where η is the ratio of the radius of the current loop to the length of the film. For a detailed derivation of Eq. (1) and the magnetic term described by Eq. (2), see [8]. Note that if we remove the term $\lambda f(x)$, the remaining equation describes the evolution of a thin film under the external action of gravity only. This reduced equation, or some close variant of it, appears in a number of previous studies. For instance, in [12], this exact equation is studied, albeit with different boundary conditions than we will employ here. Similar models are also developed in [13,14]; in these studies the analysis is complicated by the addition of an equation for surfactant transport coupled to the evolution equation. In [15], the effect of an electric field on a thin film is explored — the evolution equation presented takes a similar form, and is coupled to an equation for the electric potential in the region of space outside the film.

Eq. (1) falls under the category of fourth order degenerate diffusion equations, which arise through the lubrication approximation. Several papers have analyzed these types of equations in a general setting, examples include [16,17]. The issues addressed in these papers appear in the present work as well. Note however, that in these studies the evolution equation analyzed is autonomous. The addition of the non-autonomous function $f(x)$ to the thin film equation greatly changes the film behavior and also complicates some standard techniques of analysis; the effect of this added function is a key element of our analysis.

The domain of the film is $0 \le x \le 1$, where $x = 0$ corresponds to the top of the film and the location of the current loop, and $x = 1$ is the bottom of the film. Note that the term inside the x derivative is the velocity flux $Q(x, t)$ over a horizontal cross section; that is

$$Q(x,t) = \frac{h^3}{3}\left[\sigma h_{xxx} + 1 + \lambda f(x)\right].$$

There are several options for boundary conditions, depending on the specifics of the experiment. In [8], experiments consist of a film formed over an isolated rectangular frame. Hence, the natural boundary conditions, which we use in this paper, are

$$h(0,t) = h(1,t) = 1, \qquad Q(0,t) = Q(1,t) = 0. \tag{3}$$

Physically, the assumption is that the film is pinned to the frame and there is no flux across the frame at either end. Note that the no-flux condition implies a volume conservation.

Our objective in this paper is to analyze the system given by Eq. (1) with boundary conditions (3). We begin in Section 2 with a numerical investigation. A key characteristic that emerges is that all solutions approach steady state equilibrium profiles. In Section 3, we study analytically these equilibrium solutions. An interesting aspect is that piecewise equilibrium solutions may be constructed, which by their nature contain singularities in the third derivative. We prove several theorems regarding the construction and validity of equilibrium solutions, and how the shape of the forcing function $f(x)$ dictates the shape of equilibrium profiles. This analysis is conducted for an arbitrary forcing function. In Section 4, we numerically explore the convergence of different solution profiles to a steady state profile as well as their stability. We also illustrate the rich structure of the solution set, and consider the evolution and bifurcation of solutions as the magnetic field strength is altered.

2. Numerical solution

We begin with numerical simulations of the system (1)–(3), using the method of lines. Motivated by the zero flux boundary

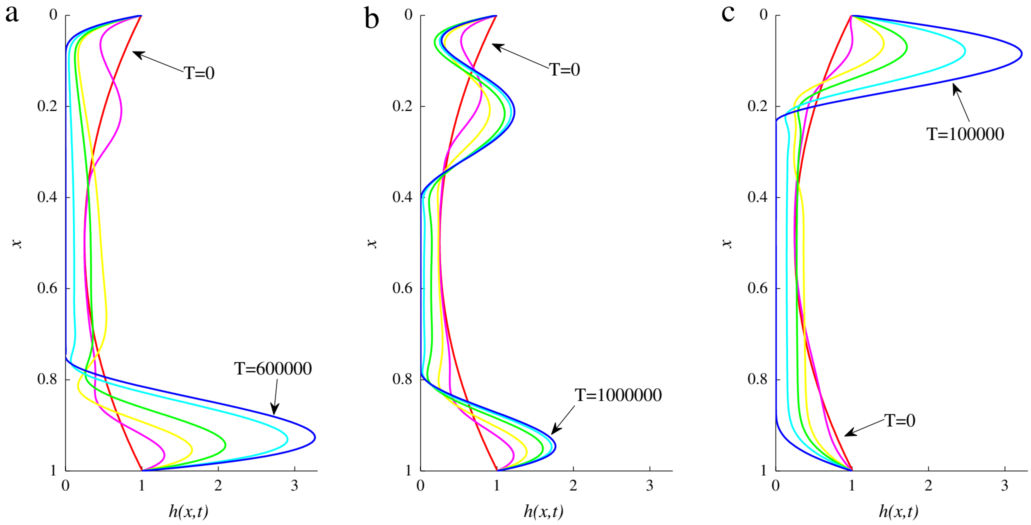

Fig. 2. Evolution of the film starting with a parabolic initial profile. In (a), $\lambda = 1$ — a relatively weak magnetic field strength; in (b), $\lambda = 1.9$ — a magnetic field of intermediate strength; and in (c) $\lambda = 5$ — a relatively strong magnetic field. In each case, $\sigma = 0.001$, and $\eta = 1$.

conditions and volume conservation, we use a conservative numerical scheme, second order in time and space, to solve the evolution equation for the free surface. The interior of the domain x between 0 and 1 is discretized as $x_i = id - d/2$, $i = 1, 2, \ldots, N$, where $d = 1/N$ is the step size for N the number of interior spatial grid points. Eq. (1) can be written as

$$\frac{\partial h}{\partial t} = -\frac{\partial Q}{\partial x}, \tag{4}$$

with boundary conditions $h = 1$ and $Q = 0$ at $x = 0, 1$. Using this representation, we determine $\frac{\partial h}{\partial t}$ at each interior point x_i by computing the flux Q one half step forward and one half step backward, i.e.

$$\frac{\mathrm{d}h_i}{\mathrm{d}t} = -\frac{Q_{i+1/2} - Q_{i-1/2}}{d}, \qquad Q_{i\pm 1/2} = Q(x_{i\pm 1/2}) \tag{5}$$

where $h_i = h(x_i)$. Centered finite difference formulas are used to compute Q at the half steps, with appropriate imbalanced difference formulas at the ends. Observe that due to the grid spacing, the flux one half step backward (forward) from x_1 (x_N) is automatically determined by the boundary conditions $Q = 0$ at the ends. The resulting system of ordinary differential equations for the h_i at the grid points is then solved using ODE15s, which is MATLAB's stiff solver. Convergence tests, performed with grid sizes from $N = 100$ to $N = 800$, produced consistent results with different values of N and different relative and absolute tolerances. The simulations shown in this article use a relative tolerance of 10^{-5} and an absolute tolerance of 10^{-8}, with $N = 200$ or $N = 400$.

The general effect of the magnetic field is demonstrated in Fig. 2, which shows the evolution of the film profile in three different regimes: a relatively weak magnetic field ($\lambda = 1$), strong magnetic field ($\lambda = 5$), and a magnetic field of intermediate strength ($\lambda = 1.9$), with all other variables fixed. In each case, the film becomes very thin in certain places, with $h(x, t)$ getting very close (but not equal) to zero (on the order of 10^{-3}) — this corresponds to the formation of black film. With a weak magnetic field, the film drains downwards with the black film forming at the top. Just the opposite occurs with the strong magnetic field, and the intermediate field leads to black film forming in the middle. This trend corresponds qualitatively with experimental observation [8].

The other observation from these simulations is that in each case, the profile appears to be approaching a steady state shape. For this reason, we develop a classification of all equilibrium solutions in Section 3.

3. Equilibrium analysis

Motivated by the numerical results, in this section we study equilibrium solutions of the system. Setting the time derivative to zero in Eq. (1), we have

$$\frac{\partial}{\partial x}\left(\frac{h^3}{3}[\sigma h_{xxx} + 1 + \lambda f(x)]\right) = 0. \tag{6}$$

Integrating from 0 to x and using that $Q(0) = 0$, we obtain

$$h^3\,(\sigma h_{xxx} + 1 + \lambda f(x)) = 0. \tag{7}$$

This equation is to be solved with three constraints. Two are provided by the fixed height boundary conditions, the third comes from the condition $Q(1) = 0$ in the form of a volume conservation condition. That is, we require

$$h(0) = h(1) = 1, \qquad \int_0^1 h\mathrm{d}x = V. \tag{8}$$

Eq. (7) suggests that we look for solutions of the ODE

$$\sigma h_{xxx} + 1 + \lambda f(x) = 0. \tag{9}$$

This equation may be solved exactly, with the constants of integration determined by (8). However, in order to be physically relevant, it must hold that $h(x) \geq 0$ everywhere on $0 < x < 1$; a solution that does not satisfy this condition fails the symmetry condition at the center line of the film. In light of this, we make the following definition:

Definition 1. A solution $h(x)$ is **invalid** if $h(x) < 0$ at any point on the interval $x \in (0, 1)$.

Two sample plots of $h(x)$, solutions of Eq. (9), subject to (8), are provided in Fig. 3 for different parameter values. The curve in Fig. 3(b) is invalid by Definition 1. What is the equilibrium solution in this case? Returning to Eq. (7), observe that the system admits piecewise equilibrium solutions, where $h(x)$ is either identically zero or solves (9). Hence, we consider the construction of piecewise smooth equilibrium solutions.

3.1. Constructing equilibrium solutions

Due to the piecewise nature of possible solutions to Eq. (7), there are many different types of equilibrium solutions which can be constructed. It turns out that the family of equilibrium

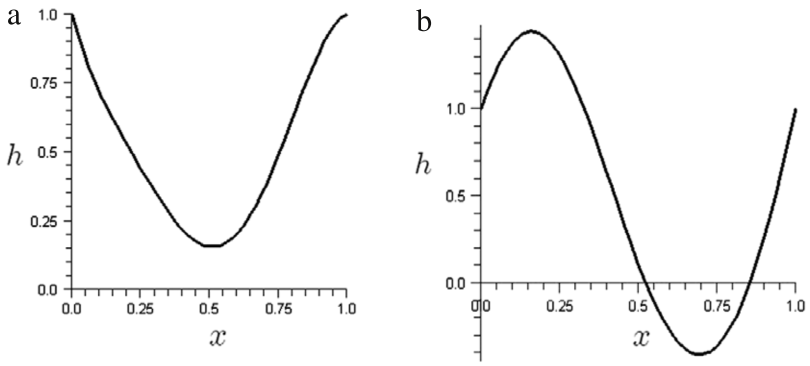

Fig. 3. Fully continuous equilibrium solutions with $\sigma = 0.004$, $\eta = 1$, $V = 0.5$, and (a) $\lambda = 1.8$, (b) $\lambda = 2.6$. The solution in (b) is invalid because $h < 0$ on $0.52 < x < 0.85$.

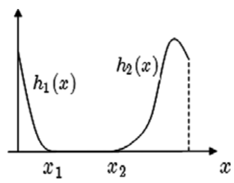

Fig. 4. Notation for equilibrium solution with a single zero-interval.

solutions possesses remarkable structure, which we uncover now and further illustrate in Section 4. It will be useful to conduct the present analysis in a more general setting. In the evolution equation, the terms $1+\lambda f(x)$ represent the sum of the scaled body forces acting on the film, in this case gravity and magnetic forces. More generally, we might consider a thin film being acted upon by an arbitrary force function $\gamma(x)$. Hence, in this section we study the following equation

$$h^3\,(h_{xxx} - \gamma(x)) = 0. \tag{10}$$

Solutions of (10) represent equilibrium solutions of a thin film acted upon by an arbitrary function $\gamma(x)$. Note also that we have removed the parameter σ, which we may assume has been absorbed into γ. Referring to Eq. (1), we would thus have $\gamma(x) = -(1+\lambda f(x))/\sigma$. For convenience, define the operator

$$L[h] = h_{xxx} - \gamma(x).$$

We first consider families of solutions for which $h = 0$ over a single interval, surrounded by two regions where h is non-zero. Following the notation of Fig. 4, we assume that $h(x) = 0$ for $x_1 < x < x_2$, which connects to the non-zero regions $h = h_1(x)$ and $h = h_2(x)$ on $0 < x < x_1$ and $x_2 < x < 1$, respectively. Each function $h_i(x)$ independently satisfies $L[h_i] = 0$.

Taking the x_i to be unknown and counting three constants of integration for each h_i gives a total of 8 unknowns. Necessary conditions to impose are

$$\begin{aligned} &h_1(0) = h_2(1) = 1\\ &h_i(x_i) = 0, \quad i = 1, 2\\ &\int_0^1 h(x)\mathrm{d}x = V. \end{aligned} \tag{11}$$

Three more conditions are needed. While there is no explicit requirement that the first derivatives match at the points x_1, x_2, our numerical simulations suggest that this degree of smoothness is necessary for a stable solution, and it is intuitively necessary to produce a physically realizable solution (we should not expect kinks in the profile). Further, at least this degree of regularity is typical in the literature (see [18], for instance), and so this is a requirement we will use throughout this analysis. Thus, we gain two more conditions by imposing $h_1'(x_1) = h_2'(x_2) = 0$. We are left one condition short. One possibility would be to require continuity of $h''(x)$ at the x_i, but note that we cannot impose this at both x_1 and x_2. Instead, we solve for the constants of integration using 6 of the conditions, saving the volume conservation condition. The volume conservation may then be treated as defining a relationship between x_1 and x_2. Explicitly, we define

$$F(x_1, x_2) := \int_0^{x_1} h_1(x)\mathrm{d}x + \int_{x_2}^1 h_2(x)\mathrm{d}x - V. \tag{12}$$

Equilibrium solutions are found by locating values of x_1, x_2 for which $F(x_1, x_2) = 0$. Any point on this curve above the line $x_1 = x_2$ represents an equilibrium solution. Note that if either of the functions $h_1(x)$ or $h_2(x)$ is concave down at the endpoints x_1, x_2, then $h(x)$ will be invalid by Definition 1. Hence, $h_i''(x_i) \geq 0$ is a necessary condition for a valid solution.

The above described construction is summarized in the following:

Hypothesis 1. Let $h(x)$ be a piecewise smooth equilibrium solution satisfying

$$h(x) = \begin{cases} h_1(x) & 0 \leq x < x_1 \\ 0 & x_1 \leq x \leq x_2 \\ h_2(x) & x_2 < x \leq 1 \end{cases} \tag{13}$$

such that $h_1(0) = 1$, $h_2(1) = 1$, $L[h_i] = 0$, and $h_i(x_i) = h_i'(x_i) = 0$ for $i = 1, 2$. By construction, x_1, x_2 will lie on the implicit curve $F(x_1, x_2) = 0$.

Under this hypothesis, we have the following theorems:

Theorem 1. *Let $h(x)$ satisfy Hypothesis 1. If in addition (x_1, x_2) corresponds to a point of horizontal tangency on the curve $F(x_1, x_2) = 0$, where F is defined in Eq. (12), then $h_1(x)$ will satisfy $h_1''(x_1) = 0$.*

The proofs for all theorems in this section are provided in Appendix A.

Theorem 2. *Let $h(x)$ satisfy Hypothesis 1. If in addition (x_1, x_2) corresponds to a point of vertical tangency on the curve $F(x_1, x_2) = 0$, where F is defined in Eq. (12), then $h_2(x)$ will satisfy $h_2''(x_2) = 0$.*

Theorems 1 and 2 imply that the points on the curve $F(x_1, x_2) = 0$ of horizontal and vertical tangency correspond to special equilibrium solutions for which $h''(x)$ is continuous at x_1 or x_2, respectively. In the following theorem, we show that valid solutions may only be located on portions of the curve with positive slope.

Theorem 3. *Let $h(x)$ satisfy Hypothesis 1 and $F(x_1, x_2)$ be given by Eq. (12). If $\frac{\mathrm{d}x_2}{\mathrm{d}x_1} < 0$ on the curve $F = 0$, then $h(x)$ is invalid according to Definition 1. Equivalently, $\frac{\mathrm{d}x_2}{\mathrm{d}x_1} \geq 0$ is a necessary condition for $h(x)$ to be a valid solution.*

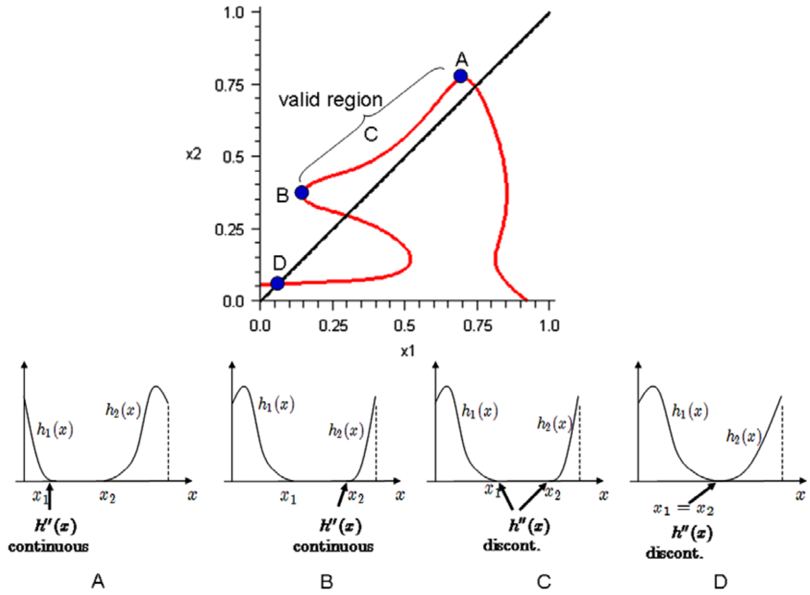

Fig. 5. Sample plot of the curve $F(x_1, x_2) = 0$ for the specific forcing function $\gamma(x) = -(1 + \lambda f(x))/\sigma$. Also a schematic for the location and form of solutions satisfying Hypothesis 1 under Theorems 1–3.

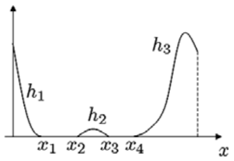

Fig. 6. Notation for equilibrium solution with two zero-intervals.

Using the above theorems, we can classify the solution structure by examining the shape of the curve $F(x_1, x_2) = 0$. A sample plot of $F = 0$ for our specific form of γ, $\gamma(x) = -(1+\lambda f(x))/\sigma$, is shown in Fig. 5. In general, there are three different types of solution: there are solutions for which h'' is continuous at either x_1 or x_2 (points A and B in Fig. 5), there is a family of solutions for which h'' is discontinuous at both x_i (region C), and there are solutions for which $x_1 = x_2$, which represent a profile with a single tangent point – i.e. a point where the curve is tangent to the horizontal axis – in the function $h(x)$ (point D).

The above analysis only accounts for solutions with a single interval where $h = 0$. We next consider the possibility of having more than one zero-interval. Consider the construction of a solution with two zero-intervals. Following the notation of Fig. 6, we suppose $h = 0$ on the intervals $x_1 < x < x_2$ and $x_3 < x < x_4$, and that the functions $h_i(x)$, $i = 1, 2, 3$ connect to these zero regions, where each $h_i(x)$ satisfies $L[h_i] = 0$. Counting three constants of integration for each h_i and the four values x_i gives a total of 13 unknowns. Setting $h_1(0) = h_3(1) = 1$, and $h_i = h_i' = 0$ at the x_i's gives 10 conditions, with volume conservation providing an 11th. There are thus two free variables. Solutions are constructed in two steps as follows:

(1) We may solve for the middle solution $h_2(x)$ independently by using the conditions $h_2(x_2) = h_2(x_3) = h_2'(x_2) = 0$ to solve for the constants of integration. We then define

$$G(x_2, x_3) := h_2'(x_3), \tag{14}$$

and determine x_2 and x_3 by plotting $G = 0$, which implicitly defines a curve in the x_2–x_3 plane.

(2) Once x_2 and x_3 are determined, the procedure to find x_1 and x_4 is the same as in the single zero-interval case, with a slight modification. Here, the volume condition gives a relationship between x_1 and x_4. Explicitly, we define

$$\hat{F}(x_1, x_4) := \int_0^{x_1} h_1 \mathrm{d}x + \int_{x_2}^{x_3} h_2 \mathrm{d}x + \int_{x_4}^{1} h_3 \mathrm{d}x - V \tag{15}$$

and determine solutions as values of x_1, x_4 for which $\hat{F} = 0$, and such that $x_1 < x_2$ and $x_4 > x_3$. To summarize, we now consider solutions which satisfy the following:

Hypothesis 2. Let $h(x)$ be a piecewise smooth equilibrium solution satisfying

$$h(x) = \begin{cases} h_1(x) & 0 \le x < x_1 \\ 0 & x_1 \le x \le x_2 \\ h_2(x) & x_2 < x < x_3 \\ 0 & x_3 \le x \le x_4 \\ h_3(x) & x_4 < x \le 1 \end{cases} \tag{16}$$

such that $h_1(0) = 1$, $h_3(1) = 1$, $L[h_i] = 0$ for $i = 1, 2, 3$, $h_1(x_1) = h_1'(x_1) = h_3(x_4) = h_3'(x_4) = 0$, and $h_2(x_i) = h_2'(x_i) = 0$ for $i = 2, 3$. By construction, x_2, x_3 will lie on the implicit curve $G(x_2, x_3) = 0$, and x_1, x_4 will lie on the implicit curve $\hat{F}(x_1, x_4) = 0$.

Note that having found and chosen values for x_2 and x_3, the curve $\hat{F} = 0$ is identical to the curve $F = 0$, but with the volume decreased to account for the added mass of the solution h_2. Hence, Theorems 1–3 apply for this case as well.

There are several different types of solution satisfying Hypothesis 2. Taking all x_i to be distinct values yields a solution with two separate zero-intervals. From the results of Theorems 1 and 2, these solutions may or may not have continuity of h'' at x_1 and x_4, based on the location of x_1, x_4 on the curve $\hat{F} = 0$. If $x_1 = x_2$ or if $x_4 = x_3$, the resulting solution will have a single tangent point and a single zero-interval, and if both $x_1 = x_2$ and $x_4 = x_3$, the solution will have two tangent points. Taking $x_3 \to x_2$ reduces the solution back to a single zero-interval, and equality of all four x_i gives a solution with a single tangent point. In general, solutions which contain an interval really consist of a family of such solutions, since they will lie on the continuum of a curve. So, for instance, the boundary of the family of curves with two zero-intervals is typically a solution with an interval and a tangent point. Hence, we should expect to see a coherent structure and relationship between the different solutions. We return to this idea in Section 4.

Next, we consider the middle section $h = h_2(x)$, and the curve $G(x_2, x_3) = 0$. Due to the symmetric nature of x_2 and x_3, the curve is symmetric about the line $x_2 = x_3$. Similar to results for the curve $F(x_1, x_2) = 0$, Theorem 4 below tells us that points of vertical and horizontal tangency mark special solutions, and provide boundaries for where valid solutions satisfying $h''(x_i) \geq 0,\ i = 2, 3$ may be found.

Theorem 4. *Let $h(x)$ satisfy Hypothesis 2. At a point of vertical tangency of the curve $G(x_2, x_3) = 0$, where G is defined by Eq. (14), $h_2(x)$ will satisfy $h_2''(x_3) = 0$. At a point of horizontal tangency, it will hold that $h_2''(x_2) = 0$.*

We now turn to the question of how the form of $\gamma(x)$ dictates the form of the curve $G = 0$ and validity of solutions. First, note that $G(x, x) = 0$ for all x; that is, the diagonal $x_2 = x_3$ is always part of the curve $G = 0$, representing a trivial solution.

Theorem 5. *Assuming that $\gamma \in C^2(\mathbb{R})$ and that $\gamma'(x^*) \neq 0$, a non-trivial branch of the curve $G = 0$, defined in Eq. (14), intersects the diagonal $x_2 = x_3$ at x^*, if and only if $\gamma(x^*) = 0$.*

As the above theorem indicates, each root x^* of $\gamma(x)$ corresponds to a branch of $G = 0$ that intersects the line $x_2 = x_3$ at x^*. The following result shows that those branches for which $\gamma'(x^*) > 0$ represent valid solutions, while branches for which $\gamma'(x^*) < 0$ represent invalid solutions.

Theorem 6. *Let x^* be a root of $\gamma(x)$, and let $h(x)$ be a solution satisfying Hypothesis 2 that corresponds to a point (x_2, x_3) on the branch of the curve $G = 0$ connecting to the point (x^*, x^*). Then, when the hypotheses of Theorem 5 are satisfied, $h(x)$ is valid (at least on the portion (x_2, x_3)) if $\gamma'(x^*) > 0$, and invalid if $\gamma'(x^*) < 0$.*

3.2. Specific form of $\gamma(x)$

The theorems of Section 3.1 provide information on the structure of equilibrium solutions for an arbitrary forcing function $\gamma(x)$ based on the shape of γ and the implicit curves $F = 0$, $\hat{F} = 0$, and $G = 0$. We now return to the specific evolution Eq. (1) where $\gamma(x) = -(1 + \lambda f(x))/\sigma$. A simple corollary of Theorem 5 is that if $\gamma(x)$ does not have any roots, then there can be no solutions to $G(x_2, x_3) = 0$, i.e. it is impossible to construct an equilibrium solution with a "middle region". In the case

$$\gamma(x) = -\frac{1 + \lambda f(x)}{\sigma} = \frac{3\lambda\eta^2 x}{\sigma(1 + \eta^2 x^2)^4} - \frac{1}{\sigma}, \tag{17}$$

$\gamma(x)$ only has a single extremum, and one can show that $\gamma(x) \leq 0$ on $0 < x < 1$, and thus no "middle region" is possible, if

$$\lambda \leq \lambda^* = \frac{8^4}{3\eta 7^{7/2}}. \tag{18}$$

When $\lambda > \lambda^*$, $\gamma(x)$ has two roots. The slope is positive at the smaller root and negative at the larger value; hence by Theorem 6, the lower branch of the curve $G = 0$ gives valid solutions and the upper branch leads to invalid solutions. This is depicted schematically with a sample plot of $G = 0$ in Fig. 7.

The final aspect we consider is how many "middle regions" are possible. When $\gamma(x)$ takes the form (17), we have the following.

Theorem 7. *For the specific form of $\gamma(x)$ given by Eq. (17), it is impossible to have more than one middle region. Put differently, at most two zero-intervals may exist.*

4. Structure of equilibrium solutions

In the previous section, we analyzed the construction of equilibrium solutions. In particular, we found that there are potentially multiple (and even infinitely many) equilibrium solutions for a fixed parameter set. The analysis of the previous section was conducted for a general forcing function. For the remainder of the paper, we restrict our attention to the specific system with forcing function given by Eq. (17).

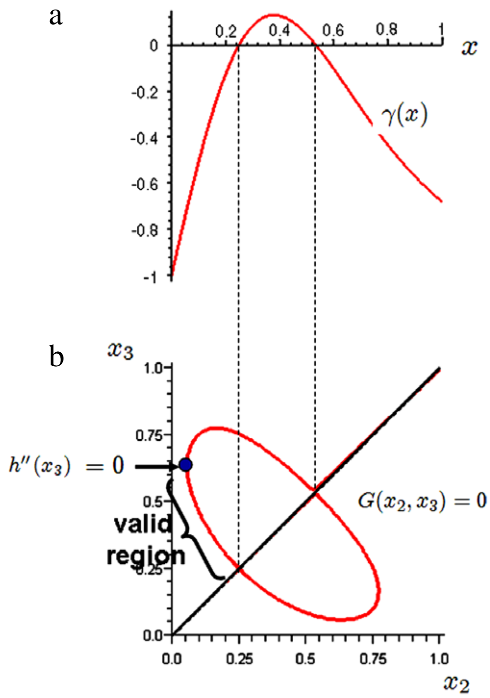

Fig. 7. (a) Sample plot of $\gamma(x) = -(1 + \lambda f(x))/\sigma$ for $\lambda = 1.7$, $\eta = 1$, $\sigma = 1$, and (b) the corresponding curve $G(x_2, x_3) = 0$. Theorems 4–6 are seen schematically by the relationship between $\gamma(x)$ and $G = 0$ and the location of valid solutions.

It is important to note that any piecewise equilibrium solution is singular, since there is at least one discontinuity in the second derivative $h''(x)$. Also, these solutions are physically unrealizable, in that $h = 0$ represents self-intersection of the film. We conjecture, however, that singular equilibrium solutions are attainable as time goes to infinity. This claim likely requires a weak formulation in order to prove — this type of approach is presented for similar but autonomous systems in [19,17,20]. Such an analysis goes beyond the scope of this manuscript, but Section 4.1 provides numerical evidence to support this claim.

Our simulations have indeed demonstrated that these equilibrium solutions appear to be locally stable, in the sense that an initial profile "close" to an equilibrium solution will return to that equilibrium solution as $t \to \infty$. Stability of equilibrium solutions is somewhat difficult to study due to their piecewise nature and the physical requirement that $h \geq 0$. Even choosing a perturbation is not trivial since it must be volume preserving, without causing the function to be negative anywhere. It does seem, however, that every equilibrium solution is stable, and has a unique zone of attraction.

As shown in Section 3, multiple (and even infinitely many) equilibrium solutions potentially exist for a given set of parameters, with varying degrees of regularity. One might intuitively think that the most regular solution should be the only stable solution, but this is evidently not the case. A quick example is provided in Fig. 8, which shows the initial and final profiles for a fixed set of parameters. We used perturbations from a piecewise equilibrium solution as initial profiles, and integrated the system forward to a large time. For the parameters used, a fully continuous non-piecewise equilibrium solution exists, whereas the equilibrium solution perturbed from has two discontinuities in the second derivative. In the first plot, the perturbation is relatively small, and the profile

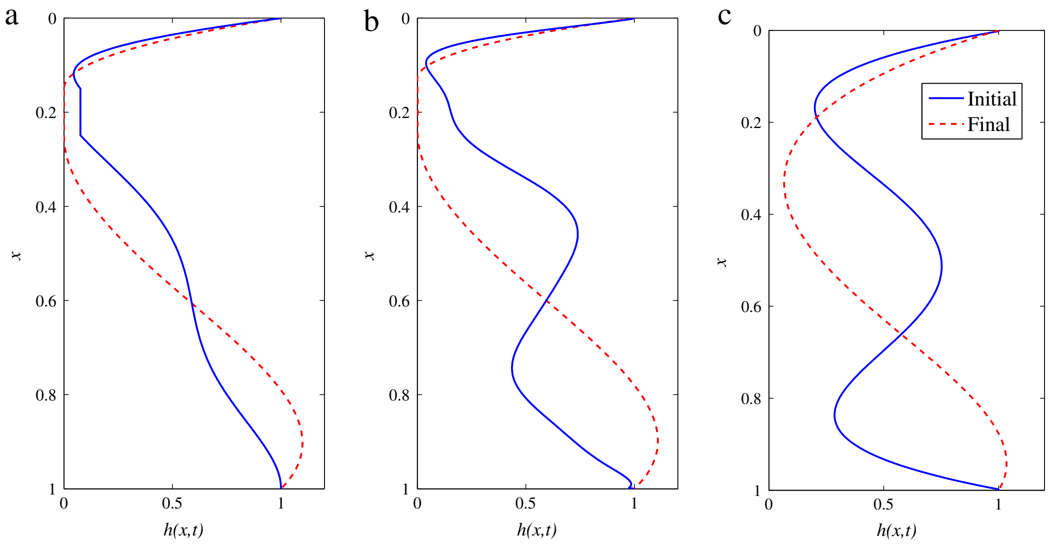

Fig. 8. Plot of initial (solid line) and final (dotted line) profiles for varying initial profiles. Parameters are $\lambda = 1, \sigma = 0.01, \eta = 1$.

returns to the piecewise solution. In the second plot, the perturbation is fairly significant, so that the initial profile looks no more like the piecewise solution than the non-piecewise solution. Still, the profile returns to the piecewise solution. In the third plot, a very large perturbation is used, and finally the profile is attracted to the continuous non-piecewise solution. Again, we leave a formal analysis of stability for future work.

4.1. Convergence to equilibrium solutions

We now turn to the convergence of numerical solutions to singular equilibrium solutions. Convergence is rather slow and appears to be algebraic in time (i.e. $\|h(x,t) - h_{\text{exact}}(x)\| \sim 1/t^p$, although the exponent p seems to vary with the parameter λ). We studied convergence in the L^2, H^1, and H^2 norms by approximating the relevant integrals with second order discretizations, using either the midpoint or the trapezoidal rule. More precisely, given a function $u(x,t)$ defined for $x \in [0, 1]$ and $t \geq 0$, we introduce the following norms:

$$L^2 \text{ norm: } \left[\int_d^{1-d} u(x,t)^2 \mathrm{d}x\right]^{1/2},$$

$$H^1 \text{ norm: } \left[\int_d^{1-d} \left(u(x,t)^2 + \left(\frac{\partial u}{\partial x}(x,t)\right)^2\right) \mathrm{d}x\right]^{1/2},$$

$$H^2 \text{ norm: } \left[\int_d^{1-d} \left(u(x,t)^2 + \left(\frac{\partial u}{\partial x}(x,t)\right)^2 + \left(\frac{\partial^2 u}{\partial x^2}(x,t)\right)^2\right) \mathrm{d}x\right]^{1/2}.$$

Here, $d = 1/N$ is a small parameter and the function $u(x,t)$ or its derivatives are known at a finite number of equally spaced values of $x \in [0, 1]$, given by $u_i = u(x_i, t)$ with

$$\text{(P1)} \quad \left\{x_i = \frac{d}{2} + (i-1)d,\ i = 1, 2, \ldots, N\right\},$$

$$\text{or (P2)} \quad \{x_i = i\,d,\ i = 1, 2, \ldots, N-1\}.$$

Each term in the above integrals is approximated numerically to order d^2, either with the midpoint rule (if $x_i = d/2 + (i-1)d$) or the trapezoid rule (if $x_i = i\,d$). Note that the function $h(x,t)$ is known at points of type (P1) and its spatial partial derivatives are defined at points of type (P2). This, together with the requirement of having second order approximations of the norms, constrains the choice of the limits of integration. The values d and $1-d$ (instead of 0 and 1) were selected in order to have the same limits of integration for all of the norms defined above. The left panel of Fig. 9 shows the behavior of the norms of the difference between the numerical solution $h(x,t)$ and an exact stationary solution $h_{\text{exact}}(x)$ for $\lambda = 3$, $\eta = 1, \sigma = 0.004$, and $V = 0.5$, where V is the volume of the film. In this case, the exact solution has only one point of discontinuity in the second derivative, and the positions of $x_1 \simeq 0.5222$ and $x_2 \simeq 0.5812$ are dictated by the parameters. The convergence in the H^2 norm is not very good because the second derivative of h_{exact} has a jump of size about 45.0 at $x = x_1$. The numerical solution tries to interpolate between each side of the jump, thereby introducing local errors of order one. However, we have checked that at longer times (and with an increased number of points to reduce numerical errors), the H^2 norm also decreases algebraically. Moreover, Fig. 10 shows the numerical and the exact solutions, as well as their first and second derivatives, at different times throughout the simulation of Fig. 9. It is clear from this figure that even though the H^2 norm of the difference between the numerical and exact solutions is still of order one, the graphs of these two solutions are already reasonably close to one another at $t = 3 \cdot 10^6$.

The right panel of Fig. 9 shows convergence of the numerical solution to an exact solution for which $x_1 = x_2$. In this case, the jump in the second derivative of h is smaller and the convergence in the H^2 norm is therefore better. The parameters are the same as above, except that $\lambda = 1.3$. The singular solution has $x_1 = x_2 = x_d$, with $x_d \simeq 0.37448$, and the second derivative of h_{exact} has a small jump (of size approximately equal to 11.2) at $x = x_d$.

Movies showing the time evolution (from $t = 0$ to $t = 3 \cdot 10^6$) of the numerical solution and its first three derivatives are provided in the supplemental material, for the two values of λ mentioned above, as well as for $\lambda = 0.4$. For $\lambda = 1$ and $\lambda = 2.8$, a figure similar to Fig. 9 illustrates the fact that the exponent p varies with λ.

4.2. Bifurcation diagrams

Having established their construction and convergence properties, we now consider how the structure of equilibrium solutions is altered as we vary the parameter λ. One might ask similar questions for the other parameters; however, from a physical standpoint, it seems most reasonable to study the effect of λ, as the

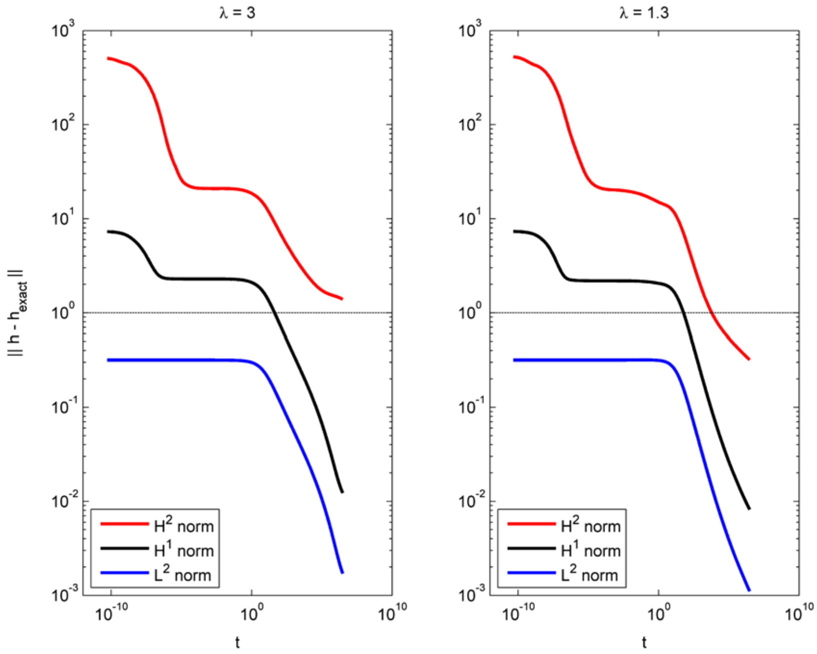

Fig. 9. Convergence of the numerical solution towards an exact solution, for $\lambda = 3$ (left panel) and $\lambda = 1.3$ (right panel). The log–log plots show the behavior of the L^2, H^1, and H^2 norms of the difference $\|h(x,t) - h_{\text{exact}}(x,t)\|$ as functions of time. Other parameters are $\eta = 1$, $\sigma = 0.004$, $V = 0.5$, $N = 400$, and the forcing is given by Eq. (17).

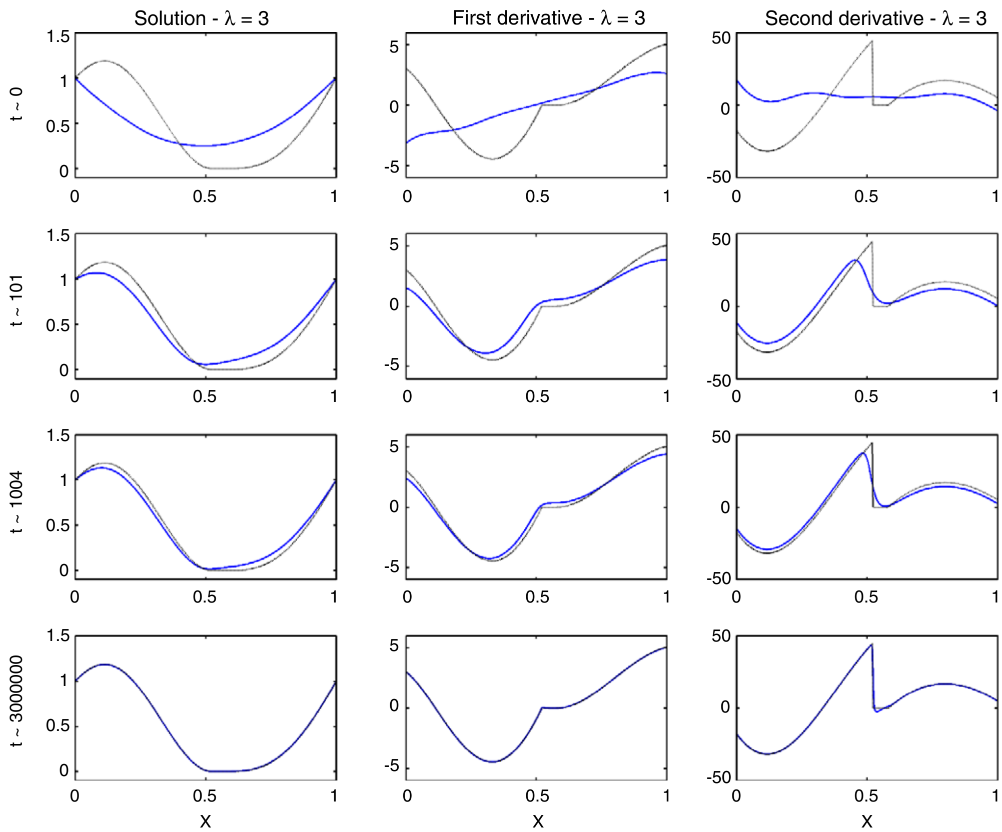

Fig. 10. Convergence of the numerical solution towards an exact solution, for $\lambda = 3$. The numerical (solid curves) and exact (dashed curves) solutions and their first and second derivatives are shown at different times of the simulation. The parameters are the same as for the left panel of Fig. 9.

magnetic field strength is the most tunable parameter. As we have seen, the solution set is completely determined by the shape of the curves $G = 0$, $\hat{F} = 0$, and $F = 0$, as described in Section 3. One way to see the evolution, then, is to follow how these curves change as λ is varied. This is not an appealing option, though, because it does not provide a very compact description of the structure. As an alternative, we may track the location of the endpoints of the zero-intervals. That is, we can consider bifurcation diagrams which plot the location of the zeros x_i as a function of λ. The difficulty here is that, as we have seen, many of the solutions lie on a curve, and so the zeros actually form a continuum for a fixed λ. Rather than try to include the entire continuum, which would clutter up a

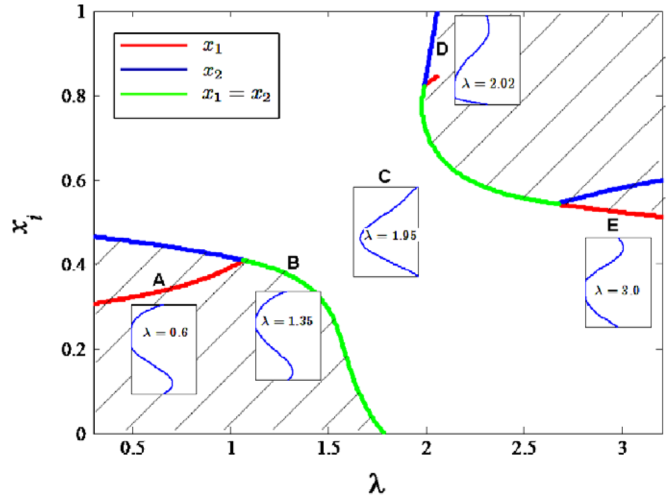

Fig. 11. Bifurcation diagram of the structure of piecewise smooth equilibrium solutions, for the parameters $\sigma = 0.004$, $\eta = 1$, and $V = 0.5$, and $\lambda \in (0.4, 3.1)$. The curves follow the locations of the zeros x_i, which provide boundaries for the regions of valid solutions, depicted by the shaded areas. The insets show the shape of solution profiles for different regions. (For interpretation of the references to colour in this figure legend, the reader is referred to the web version of this article.)

bifurcation diagram, we follow the boundaries of the regions of valid solutions.

Such a bifurcation diagram is provided in Fig. 11, for the parameters $\sigma = 0.004$, $\eta = 1$, and $V = 0.5$, and $\lambda \in (0.4, 3.1)$. Following the notation of Fig. 4, the red line is the location of x_2, the blue line the location of x_1, and the green line follows the tangent solutions where $x_2 = x_1$. Note that the red and blue lines are linked — each value of x_1 on the red line is paired with a value of x_2 on the blue line for a given value of λ; the pair (x_1, x_2) defines the end points of the zero-intervals of a specific solution for which $h''(x)$ is continuous at one of the x_i. As stated, these curves are the boundaries for valid solution regions. Values of x_1, x_2 corresponding to the interior of the continuum (for which $h''(x)$ is discontinuous at both x_1 and x_2) are found in the shaded regions. Also included in the plot are solution profiles corresponding to the different regions of the diagram.

Viewed in this format, an interesting structure emerges. Near the left edge of the diagram, when λ is smaller, the bulk of the film has drained to the bottom, and a solution satisfying $h''(x_1) = 0$ exists (branch A in Fig. 11). For this portion of the diagram, physically gravity is dominating the magnetic force. As λ is increased, the x_1 and x_2 values for this solution coalesce to a tangent solution (branch B). This tangent solution eventually disappears, the tangent point going to $x_1 = x_2 = 0$. Then, for $1.78 < \lambda < 1.98$, there are no piecewise equilibrium solutions. The only solution present in this interval is the fully continuous solution, seen in region C. At $\lambda = 1.98$, a bifurcation occurs whereby two tangent solutions appear. The upper branch bifurcates again, with x_2 splitting away from x_1 — this branch of solutions then disappears when x_2 hits the boundary $x_2 = 1$ (branch D). Due to the linked nature of the curves, at this point the red line must also disappear. The lower branch of tangent solutions bifurcates at $\lambda \approx 2.68$, into a solution with $h''(x_2) = 0$ (branch E). For this branch of solutions, the bulk of the film has now drained upwards — for this portion of the diagram the magnetic force is dominating gravity. If we were to extend the diagram for larger λ, this branch of solutions would remain, with x_1 and x_2 spreading further apart as the thin region got larger and larger with more and more film draining upwards.

For the parameters above, no solutions with two zero-intervals exist. However, by decreasing the value of σ from $\sigma = 0.004$ to $\sigma = 0.001$, the structure of solutions changes rather dramatically. In particular, following the notation of Section 3, when $\sigma = 0.004$, there are no valid solutions to the equation $\hat{F}(x_1, x_4) = 0$, defined in Eq. (15) for any (x_2, x_3) on the curve $G = 0$ (see Eq. (14)); hence the absence of solutions with two zero-intervals. With $\sigma = 0.001$ however, solutions with two zero-intervals do appear for certain values of λ. The bifurcation diagram for this case is given in Fig. 12. Fig. 12(a) shows only the solutions with a single interval, and the structure is similar to that of Fig. 11. Fig. 12(b) shows the full diagram — as there are two zero-intervals in this case, we track the location of x_i, $i = 1, \ldots, 4$, following the notation of Fig. 6.

The details of this diagram are far more complicated in terms of how solution types are structured. For instance, the two branches marked A, where $x_1 = x_2$ and $x_3 = x_4$, represent solutions with two tangent points. The branches marked B represent a boundary for solutions with a single tangent point, with $x_3 = x_4$, and an interval. The branch marked C provides the boundary for solutions with two zero-intervals, because on this curve the middle region collapses to a point with $x_2 = x_3$. As solutions are defined by separate continuous curves, $G = 0$ and $\hat{F} = 0$, locating regions of valid solutions is very complicated. Nevertheless, while individual solutions are difficult to decipher from this diagram, the coherent structure and connection of the equilibrium solutions is more than apparent.

Finally, given that multiple stable equilibria are possible, and having seen the intricate structure of the bifurcation diagrams, we consider how the film profile might traverse this diagram. Envision the following experiment: allow the film to drain until it is reasonably close to a steady state. Then, change the strength of the magnetic field by altering the current in the current loop. The film is no longer in equilibrium and the profile will move towards a new equilibrium. If we continue to gradually change the strength of the field, how will the steady state film profile transition through the landscape of possible equilibrium solutions?

To explore this, we can conduct the equivalent numerical experiment. Starting from a parabolic profile, we integrate forward to some large time T. We then change λ by a small amount, use the ending profile as an initial profile for the new λ, integrate forward to T again, and repeat this process over some range of λ. By plotting the locations of the discontinuities of the second derivative of the numerical solution at each λ, we can infer the values of the x_i's, and thus how the profile is traversing the bifurcation diagram of equilibrium solutions. We performed this numerical experiment for the bifurcation diagram of Fig. 11. We used 30 equally spaced values of λ over the range $[0.49, 2.9]$. The result appears in Fig. 13. Fig. 13(a) plots the location of the x_i's as λ is increased starting from $\lambda = 0.49$; Fig. 13(b) plots the x_i's as λ is decreased starting from $\lambda = 2.9$. Some interesting behavior can be seen. First, note that the most regular piecewise solutions are the ones directly on the solid lines, because for these solutions $h''(x)$ is only discontinuous at a single point, whereas the solutions which lie in the interior of the continuum of solutions will have two points of discontinuity of $h''(x)$. Nevertheless, following Fig. 13 from left to right, the profile leaves the solid line by the second point, meaning that the profile is being attracted to a solution with two points of discontinuity in $h''(x)$ instead of the solution with only a single point of discontinuity. Continuing, the x_i's come together as a tangent solution (the green point on the left half), after which the profile transitions to the fully continuous profile, not visible on the diagram. When the solution touches back down on the right half of the diagram, it then follows the most regular curve until the end. We might surmise, then, that the solid line solutions on the right half of the diagram are stronger attractors than on the left half. Considering Fig. 13(b), this is clearly not the case. When decreasing λ, i.e. following Fig. 13(b) from right to left, the same type of behavior occurs, in reverse. The solution jumps off the solid line initially, but then follows the most regular curve after touching back down on the left side.

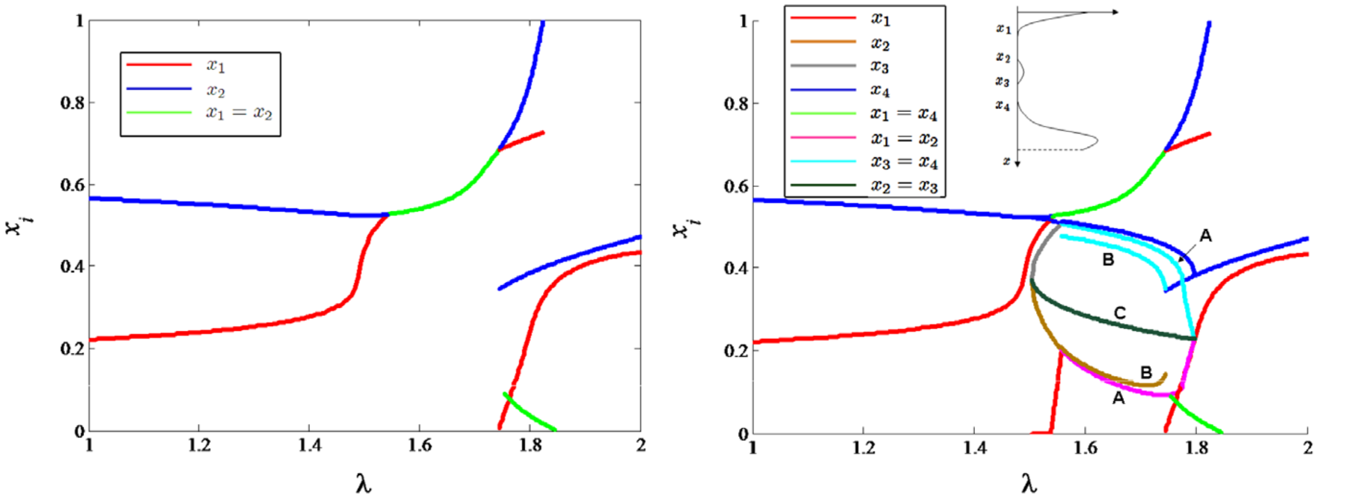

(a) The family of single interval solutions.

(b) The full diagram, including double interval solutions.

Fig. 12. Bifurcation diagram of the structure of piecewise smooth equilibrium solutions, for the parameters $\sigma = 0.001$, $\eta = 1$, and $V = 0.5$, and $\lambda \in (1, 2)$. The curves plot the locations of the zeros x_i. (a) shows only solutions with a single zero-interval, (b) also includes solutions with two zero-intervals.

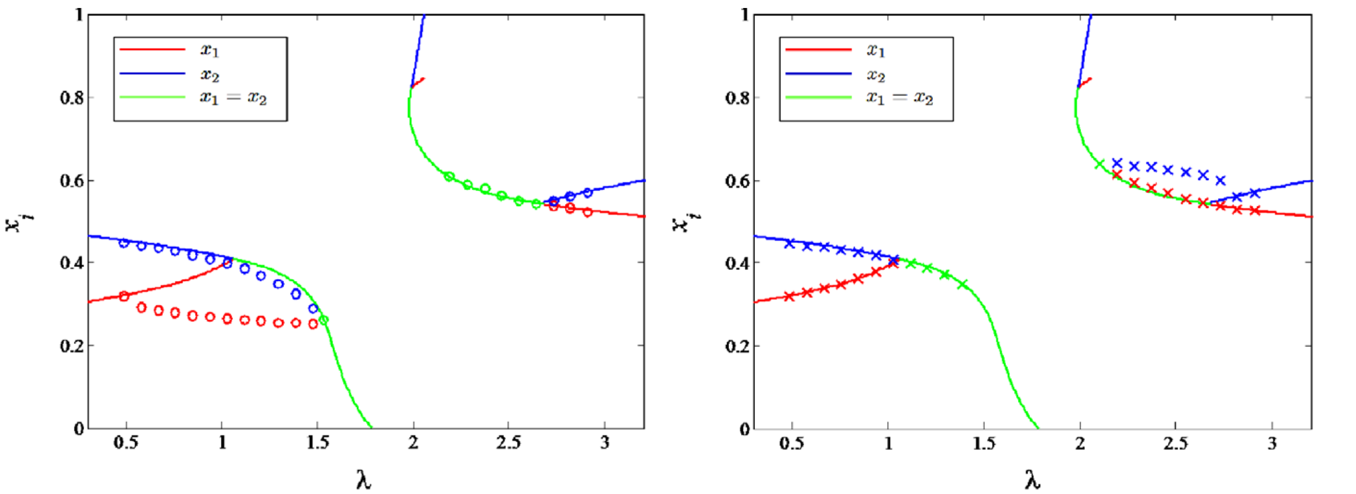

(a) Increasing λ.

(b) Decreasing λ.

Fig. 13. Results of the numerical experiment showing how the film profile traverses the field of equilibrium solutions. Parameter values used were $\sigma = 0.004$, $\eta = 1$, and $V = 0.5$. In (a), λ is increased incrementally from 0.49 to 2.9, with the location of the equilibrium solution plotted at each step. In (b), the same is done for λ decreasing from 2.9 to 0.49. (For interpretation of the references to colour in this figure legend, the reader is referred to the web version of this article.)

The simulation may also be described as follows: on the left side of the diagram, where the magnetic force is generally weaker than gravity, an increase in the magnetic force causes the profile to leave the most regular solution, thereby increasing the size of the black film (the distance between x_1 and x_2 is smallest on the solid lines), while with a decrease in the magnetic force the profile remains on the most regular solution, keeping the black film as small as possible. On the right side of the diagram where the magnetic force is stronger than gravity, just the opposite occurs: an increase (decrease) in magnetic force causes the profile to remain on (leave) the most regular solution. The other interesting aspect, alluded to in this discussion, is the hysteresis effect. This simulation suggests that the film's history becomes important when altering the magnetic force.

5. Conclusion

In this paper, we presented a rigorous analysis of equilibrium solutions of the system of Eqs. (1), (3), derived in [8] as a first model for a draining magnetic soap film under the action of a non-uniform magnetic field. In studying this system, we first implemented a numerical scheme to solve the evolution equation of the thin film profile. Simulations demonstrated the qualitative effect of the magnetic field, and captured the reverse draining effect observed experimentally for strong magnets. While the model may be missing some important components, this qualitative agreement is promising and lends credence to conclusions derived from analyzing this first model.

The phenomenon of reverse draining observed in [8], and reproduced analytically here, is intriguing from a purely physical standpoint, and adds an interesting piece to the well-studied puzzle of a draining soap film. More generally, our analysis may provide a step in the direction of thin film fluid control, particularly with respect to ferrofluids. The results of Section 3 suggests that fine control of film flow and equilibrium solutions may be possible. As our analysis was conducted for an arbitrary forcing function, this point is worth further discussion. We found that the structure of equilibrium solutions relates directly to the complexity and number of

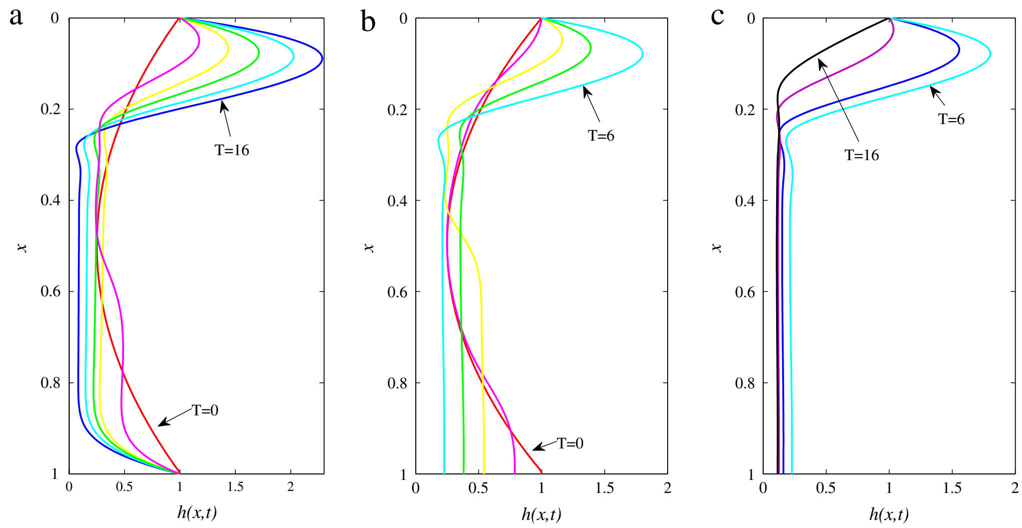

Fig. 14. Evolution of film profile using (a) — fixed height and zero flux at top and bottom and (b), (c) — fixed height and zero flux at top, but Eq. (19) at the bottom. (b) shows the first phase of the evolution, and (c) the second phase. Parameters used are $\lambda = 10$, $\sigma = 0.001$, $\eta = 1$, and $\delta = 1$.

roots of the forcing function. Physically, this is reasonable. A root of the forcing function corresponds to a point of balance of competing forces. The more roots, the more places where the sum of the body forces changes direction.

For instance, in our particular system, regions with $\gamma(x) < 0$ correspond to spatial regions where the gravitational force downwards is stronger than the magnetic force upwards, while the magnetic force is stronger in a region where $\gamma > 0$. Generally, if γ has no roots, then the force in one direction is dominant over the entire spatial region, and it is no curiosity that complex equilibrium solutions with "middle regions" are not possible. For instance, setting $\gamma = 1$ represents the case of gravity acting as the only body force. On the other hand, a forcing function γ which has multiple roots represents body forces for which the dominant direction may change multiple times over the spatial region. In such a system, we should not be surprised to find equilibrium profiles with a complex structure and even multiple "middle regions." This analysis also suggests an interesting direction for future experiments. By creating more complex magnetic fields, one could feasibly construct a γ with any shape and number of roots desired, and thus a wide range of equilibrium profiles and flow control becomes open for exploration. Due to the generality of our arguments, this exploration is not limited to magnetic fields and soap films, but could potentially be applied to any thin film system.

It must be noted, however, that the no-flux boundary conditions and volume conservation were a necessary component for many of our results. Much of our analysis was based on the construction of piecewise equilibrium solutions satisfying the general equation $h^3(h_{xxx} - \gamma(x)) = 0$. With different boundary conditions, equilibrium solutions would instead satisfy $h^3(h_{xxx} - \gamma(x)) = C$, $C \neq 0$ a constant, which does not permit piecewise solutions consisting of intervals where h is identically zero. The importance of boundary conditions is briefly illustrated in Fig. 14. Fig. 14(a) shows the evolution of a film under the boundary conditions of fixed height and zero flux that we have employed throughout this paper. In (b) and (c), we used boundary conditions of zero flux and fixed height at the top, but

$$h_{xx} = \delta, \qquad h_x = 0 \tag{19}$$

at the bottom of the film. These boundary conditions are suggested in [12] to simulate a film draining into a bath; here δ captures the size of the meniscus the film makes with the bath. Parameters used are $\lambda = 10$, $\sigma = 0.001$, $\eta = 1$, and $\delta = 1$. Fig. 14(b) shows the initial phase of the film evolution, and is qualitatively similar to that in (a). In the second phase of the evolution, however, (shown in (c)), the film cannot sustain the bulk flow upwards, and the film flows back down into the bath.

Further work with the system studied here could proceed in numerous directions. On the analytical end, a weak formulation may provide the means to offer analytical proof for the numerical results regarding convergence to a singular steady state solutions. Aside from the potential experiments mentioned above, the numerical experiment of Section 4.2 and the hysteresis observed might be easily explored in the laboratory with an electromagnet. Finally, multiple effects could be included in a future model, including surfactant transport and magnetic particle concentration.

Appendix A. Proofs of the theorems of Section 3

A.1. Proof of Theorem 1

On a point of horizontal tangency, $\frac{dx_2}{dx_1} = 0$, which implies $F_{x_1} = 0$. From Eq. (12) and using Leibniz rule, we have

$$\begin{aligned} F_{x_1} &= \frac{d}{dx_1}\int_0^{x_1} h_1(x)dx = h_1(x_1) + \int_0^{x_1} \frac{\partial h_1}{\partial x_1}dx \\ &= \int_0^{x_1} \frac{\partial h_1}{\partial x_1}dx. \end{aligned} \tag{20}$$

Define $g_1(x; x_1) = \frac{\partial h_1}{\partial x_1}$, and consider the form of g_1. Solving $L[h_1] = 0$, we may write

$$h_1(x) = \Gamma(x) + c_1x^2 + c_2x + c_3,$$

where $\Gamma'''(x) = \gamma(x)$. The boundary conditions $h_1(0) = 1$, $h_1(x_1) = h_1'(x_1) = 0$ imply that $c_3 = 1 - \Gamma(0)$ does not depend on x_1, and that

$$\begin{aligned} c_1 &= \frac{\Gamma(x_1) - \Gamma(0) + 1 - x_1\Gamma'(x_1)}{x_1^2} \\ c_2 &= \frac{-2\Gamma(x_1) + 2\Gamma(0) - 2 + x_1\Gamma'(x_1)}{x_1}. \end{aligned} \tag{21}$$

Note that since $x_1 > 0$, c_1, c_2 are at least as smooth as Γ'. We may write

$$g_1 = c_1'(x_1)x^2 + c_2'(x_1)x. \tag{22}$$

As a function of x, g_1 is quadratic. It is easily verified that $g_1 = 0$ at $x = 0$ and $x = x_1$, implying that g_1 takes only one sign on $0 < x < x_1$. Since $F_{x_1} = 0$, $\int_0^{x_1} g_1 \mathrm{d}x = 0$. Thus, g_1 is identically zero, which implies that $c_1'(x_1) = c_2'(x_1) = 0$. Next, the condition $h_1'(x_1) = 0$ may be written

$$\Gamma'(x_1) + 2c_1x_1 + c_2 = 0. \tag{23}$$

Taking a derivative with respect to x_1 across Eq. (23) and using that $h_1''(x_1) = \Gamma''(x_1) + 2c_1$, we obtain

$$h_1''(x_1) + 2c_1'(x_1)x_1 + c_2'(x_1) = 0,$$

and the result that $h_1''(x_1) = 0$ follows.

A.2. Proof of Theorem 2

This may be proven in a similar manner as Theorem 1. Briefly, $\frac{\mathrm{d}x_2}{\mathrm{d}x_1} = \infty \Rightarrow F_{x_2} = 0$, which implies that $\int_{x_2}^1 g_2 \mathrm{d}x = 0$, where $g_2 = \frac{\partial h_2}{\partial x_2}$. Writing

$$h_2(x) = \Gamma(x) + b_1x^2 + b_2x + b_3,$$

in this case the boundary conditions at $x = x_2$ and $x = 1$ imply that each $b_i = b_i(x_2)$, and so

$$g_2 = b_1'(x_2)x^2 + b_2'(x_2)x + b_3'(x_2).$$

It is easy to show that $g_2(x_2) = g_2(1) = 0$, and thus $\int_{x_2}^1 g_2 \mathrm{d}x = 0$ implies $b_i'(x_2) = 0,\ i = 1, 2, 3$. Using the condition $h_2'(x_2) = 0$ and taking a derivative with respect to x_2, we may write $h_2''(x_2) + 2b_1'(x_2)x_2 + b_2'(x_2) = 0$, and thus $h_2''(x_2) = 0$.

A.3. Proof of Theorem 3

The first step is to note the relationships

$$\begin{aligned} h_1''(x_1) &= -g_1'(x_1) \\ h_2''(x_2) &= -g_2'(x_2), \end{aligned} \tag{24}$$

which follow from the arguments used in the previous theorems. We know that $g_1(x)$ has a constant sign on $x \in (0, x_1)$. Since

$$F_{x_1} = \int_0^{x_1} g_1 \mathrm{d}x,$$

it holds that F_{x_1} has the same sign as $g_1(x)$ has on $x \in (0, x_1)$. Therefore,

$$F_{x_1} > 0 \Leftrightarrow g_1(x) > 0 \text{ on } (0, x_1) \Leftrightarrow g_1'(x_1) < 0 \Leftrightarrow h_1''(x_1) > 0. \tag{25}$$

In similar fashion, we obtain

$$F_{x_2} > 0 \Leftrightarrow g_2(x) > 0 \text{ on } (x_2, 1) \Leftrightarrow g_2'(x_2) > 0 \Leftrightarrow h_2''(x_2) < 0. \tag{26}$$

To prove the theorem, then, we need merely note that if

$$\frac{\mathrm{d}x_2}{\mathrm{d}x_1} = -\frac{F_{x_1}}{F_{x_2}} < 0$$

then F_{x_1}, F_{x_2} must have the same sign, which implies that one of $h_1''(x_1)$ or $h_2''(x_2)$ will be negative.

A.4. Proof of Theorem 4

First, we write

$$h_2(x) = \Gamma(x) + c_1x^2 + c_2x + c_3. \tag{27}$$

Imposing $h_2(x_2) = h_2(x_3) = h_2'(x_2) = 0$, we may solve for c_1 and c_2 to obtain

$$\begin{aligned} c_1 &= -\frac{1}{x_2 - x_3}\left(\Gamma'(x_2) - \frac{\Gamma(x_2) - \Gamma(x_3)}{x_2 - x_3}\right) \\ c_2 &= -\frac{1}{(x_2 - x_3)^2}\left(2x_2\Gamma(x_2) - 2x_2\Gamma(x_3) - (x_2^2 - x_3^2)\Gamma'(x_2)\right). \end{aligned} \tag{28}$$

Now, $G = 0$ is defined as $h_2'(x_3) = 0$, i.e. $\Gamma'(x_3) + 2c_1x_3 + c_2 = 0$. Using the above expressions for c_1 and c_2, we obtain after some manipulation that $G = 0$ is equivalent to

$$\Gamma'(x_2) + \Gamma'(x_3) - 2\frac{\Gamma(x_2) - \Gamma(x_3)}{x_2 - x_3} = 0. \tag{29}$$

We now compute

$$\begin{aligned} \frac{\partial G}{\partial x_2} &= \Gamma''(x_2) - 2\frac{\Gamma'(x_2)}{x_2 - x_3} + 2\frac{\Gamma(x_2) - \Gamma(x_3)}{(x_2 - x_3)^2} \\ \frac{\partial G}{\partial x_3} &= \Gamma''(x_3) + 2\frac{\Gamma'(x_3)}{x_2 - x_3} - 2\frac{\Gamma(x_2) - \Gamma(x_3)}{(x_2 - x_3)^2}. \end{aligned} \tag{30}$$

Substituting c_1 from Eq. (28) into $h_2''(x_2) = \Gamma''(x_2) + 2c_1$ and $h_2''(x_3) = \Gamma''(x_3) + 2c_1$, we find that

$$h_2''(x_2) = \frac{\partial G}{\partial x_2}, \qquad h_2''(x_3) = \frac{\partial G}{\partial x_3}, \tag{31}$$

from which the theorem immediately follows.

A.5. Proof of Theorem 5

We start with the expression of $G = 0$ given in Eq. (29),

$$\Gamma'(x_2) + \Gamma'(x_3) - 2\frac{\Gamma(x_2) - \Gamma(x_3)}{x_2 - x_3} = 0. \tag{32}$$

Define

$$g(x_3) = (x_2 - x_3)\left[\Gamma'(x_2) + \Gamma'(x_3)\right] - 2\left[\Gamma(x_2) - \Gamma(x_3)\right] \tag{33}$$

so that for a fixed x_2 and $x_3 \neq x_2$, $G = 0 \Leftrightarrow g(x_3) = 0$. Expanding $g(x_3)$ for x_3 near x_2, and using that $\Gamma'''(x) = \gamma(x)$, we obtain

$$g(x_3) = -\gamma(x_2)\frac{\epsilon^3}{3!} - 2\gamma'(x_2)\frac{\epsilon^4}{4!} + O(\epsilon^5), \tag{34}$$

where $\epsilon = x_3 - x_2$. Solving $g(x_3) = 0$ for ϵ gives, at lowest order,

$$\epsilon = \frac{-2\gamma(x_2)}{\gamma'(x_2)}. \tag{35}$$

Therefore, if a non-trivial (i.e. for which $x_2 \neq x_3$) branch of $G = 0$ exists and crosses the diagonal $x_2 = x_3$ at $x_2 = x_3 = x^*$, as the point (x_2, x_3) moves along $G = 0$ towards (x^*, x^*), we have $\epsilon \to 0$, $\gamma(x_2) \to \gamma(x^*)$, and $\gamma'(x_2) \to \gamma'(x^*) \neq 0$. As a consequence, $\gamma(x^*) = 0$. Conversely, if $\gamma(x^*) = 0$, then by writing $\gamma(x_2) = \gamma'(x^*)(x_2 - x^*) + O\left((x_2 - x^*)^2\right)$, and $\gamma'(x_2) = \gamma'(x^*) + O\left((x_2 - x^*)^2\right)$, Eq. (35) becomes

$$x_3 - x_2 = \epsilon = -2(x_2 - x^*) + O\left((x_2 - x^*)^2\right).$$

In other words, there will be a root $x_3 > x_2$ when x_2 is slightly smaller than x^* and a root $x_3 < x_2$ when x_2 is slightly larger than x^*. This implies the existence of a non-trivial branch of $G = 0$ intersecting the diagonal at x^*.

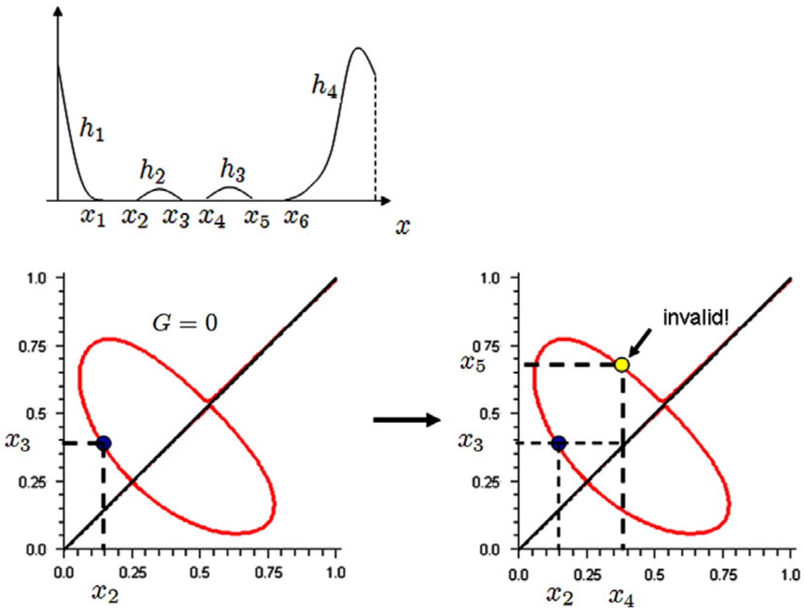

Fig. 15. Schematic proof of Theorem 7. Two middle regions are not possible, because in finding $x_2 < x_3 < x_4 < x_5$, x_4, x_5 will end up on the invalid branch, meaning that $h = h_3(x)$ will be negative at some point.

A.6. *Proof of* Theorem 6

For a given point (x_2, x_3) on $G = 0$, we have $h_2(x) = \Gamma(x) + c_1x^2 + c_2x + c_3$, with c_1 and c_2 given by Eq. (28). Using Eq. (29), these coefficients may be rewritten as

$$c_1 = -\frac{1}{2}\frac{\Gamma'(x_3) - \Gamma'(x_2)}{x_3 - x_2}, \qquad c_2 = \frac{x_3\Gamma'(x_2) - x_2\Gamma'(x_3)}{x_2 - x_3}. \tag{36}$$

A similar calculation for c_3 gives

$$c_3 = -\frac{1}{2}\left(\Gamma(x_2) + \Gamma(x_3)\right) + \frac{1}{4}\left(\Gamma'(x_2) + \Gamma'(x_3)\right)(x_2 + x_3) - \frac{1}{2}x_2x_3\frac{\Gamma'(x_3) - \Gamma'(x_2)}{x_3 - x_2}.$$

As $x_2,\ x_3 \to x^*$,

$$c_1 \to -\frac{\Gamma''(x^*)}{2}, \qquad c_2 \to x^*\Gamma''(x^*) - \Gamma'(x^*),$$

$$c_3 \to -\Gamma(x^*) + x^*\Gamma'(x^*) - \frac{x^{*2}}{2}\Gamma''(x^*),$$

and as a consequence,

$$h_2(x) = \Gamma(x) - \left(\Gamma(x^*) + \Gamma'(x^*)(x - x^*) + \frac{\Gamma''(x^*)}{2}(x - x^*)^2\right).$$

With $\gamma(x^*) = 0$ and $\gamma'(x^*) \neq 0$, a Taylor expansion of $\Gamma(x)$ near $x = x^*$ in the above equation gives, at lowest order,

$$h_2(x) \approx \frac{\gamma'(x^*)}{4!}(x - x^*)^4. \tag{37}$$

Since $h_2(x) > 0$ is the requirement for validity on (x_2, x_3), $h(x)$ is a valid solution on (x_2, x_3) if and only if $\gamma'(x^*) > 0$.

A.7. *Proof of* Theorem 7

The proof follows quickly from the shape of $\gamma(x)$, and is depicted in Fig. 15. Since γ will have at most two roots in the interval, the curve $G = 0$ will have the shape depicted in Fig. 15. As stated, the lower branch is valid and the upper branch invalid. Each middle region can be constructed in the same way — constructing two ormore middle regions comes down to whether points $x_2 < x_3 < x_4 < x_5$ may be chosen, all to lie on a valid branch of the curve. By inspection, this is not possible for γ given by Eq. (17).

Appendix B. Supplementary data

Supplementary data associated with this article can be found, in the online version, at doi:10.1016/j.physd.2009.08.014.

References

[1] L.W. Schwartz, H.M. Princen, A theory of extensional viscosity for flowing foams and concentrated emulsions, J. Colloid Interface Sci. 118 (1) (1987) 201–211.
[2] A.M. Kraynik, Foam flows, Annu. Rev. Fluid Mech. 20 (1988) 325–357.
[3] I. Newton, Opticks, S. Smith & B. Walford, London.
[4] K.J. Mysels, K. Shinoda, S. Frankel, Soap Films — Studies of their Thinning and a Bibliography, Pergamon Press, London, 1959.
[5] J.B.M. Hudales, H.N. Stein, Marginal regeneration of a mobile vertical free liquid film, J. Colloid Interface Sci. 138 (2) (1990) 354–364.
[6] H.N. Stein, On marginal regeneration, Adv. Colloid Interface Sci. 34 (1991) 175–190.
[7] V.A. Nierstrasz, G. Frens, Marginal regeneration and the Marangoni effect, J. Colloid Interface Sci. 215 (1999) 28–35.
[8] D.E. Moulton, J.A. Pelesko, Reverse draining of a magnetic soap film, Phys. Rev E (submitted for publication).
[9] F. Elias, J.-C. Bacri, C. Flament, E. Janiaud, D. Talbot, W. Drenckhan, S. Hutzler, D. Weaire, Magnetic soap films and magnetic soap foams, Colloids Surf A: Physicochem. Eng. Aspects 263 (2005) 65–75.
[10] A. Oron, S.H. Davis, S.G. Bankoff, Long-scale evolution of thin liquid films, Rev. Modern Phys. 69 (3) (1997) 931–980.
[11] R.E. Rosensweig, Ferrohydrodynamics, Cambridge University Press, New York, 1985.
[12] R.J. Braun, S.A. Snow, U.C. Pernisz, Gravitational drainage of a tangentially-immobile thick film, J. Colloid Interface Sci. 219 (1999) 225–240.
[13] L.W. Schwartz, R.V. Roy, Modeling draining flow in mobile and immobile films, J. Colloid Interface Sci. 218 (1999) 309–323.
[14] R.J. Braun, S.A. Snow, S. Naire, Models for gravitationally-driven free-film drainage, J. Engrg Math. 43 (2002) 281–314.
[15] D. Tseluiko, D.T. Papageorgiou, Nonlinear dynamics of electrified thin liquid films, SIAM J. Appl. Math. 67 (5) (2007) 1310–1329.
[16] A.L. Bertozzi, Symmetric singularity formation in lubrication-type equations for interface motion, SIAM J. Appl. Math. 56 (3) (1996) 681–714.
[17] A.L. Bertozzi, M. Pugh, The lubrication approximation for thin viscous films: Regularity and long-time behavior of weak solutions, Commun. Pure Appl. Math. 49 (2) (1996) 85–123.
[18] R.S. Laugesen, M.C. Pugh, Properties of steady states for thin film equations, European J. Appl. Math. 11 (2000) 293–351.
[19] F. Bernis, A. Friedman, Higher order nonlinear degenerate parabolic equations, J. Differential Equations 83 (1990) 179–206.
[20] A.L. Bertozzi, M.P. Brenner, T.F. Dupont, L.P. Kadanoff, Singularities and similarities in interface flows, in: Trends and Perspectives in Applied Mathematics, Springer, New York.